https://doi.org/10.5194/gmd-2023-4
Preprint. Discussion started: 9 March 2023

Geoscientific Model Development
Discussions

Adjoint of GEOS-Chem model by supporting HEMCO emission inventories and MERRA-2 meteorological data

Zhaojun Tang[1], Jiaqi Chen[1], Panpan Yang[1], Zhe Jiang[1]*

[1]School of Earth and Space Sciences, University of Science and Technology of China, Hefei, Anhui, 230026, China.

*Correspondence to: Zhe Jiang (zhejiang@ustc.edu.cn)

Abstract

Adjoint of the GEOS-Chem model has been widely used to constrain the sources of various atmospheric pollutants. Here we provide an updated version (GC-Adjoint-HEMCO) of the adjoint of GEOS-Chem model to support the MERRA-2 meteorological data and Harmonized Emissions Component (HEMCO) emission inventories. State-of-the-art inventories, such as CEDS (Community Emissions Data System), MIX, NEI2011 (National Emissions Inventory), and GFED4 (Global Fire Emission Database), are supported in GC-Adjoint-HEMCO. We find good agreements in carbon monoxide (CO) emissions from various inventories, chemical sources and sinks, and surface and column CO concentrations between GC-Adjoint-HEMCO and GEOS-Chem (v12-8-1) forward simulations. Furthermore, observing system simulation experiments (OSSE) are employed to evaluate the performance of GC-Adjoint-HEMCO in 4D variational (4D-var) assimilations. We find underestimations by approximately 15% in the a posteriori anthropogenic CO emissions over North America and Europe due to limited coverage of observations by smoothing the pseudo-CO observations with Measurement of Pollution in the Troposphere (MOPITT) averaging kernels. As an example application of GC-Adjoint-HEMCO, we constrain anthropogenic CO emissions in 2015 by assimilating MOPITT CO observations. The a posteriori anthropogenic CO emission estimates derived in this work match well with Jiang et al. (2017) in North America and Africa but are overestimated in Asia, South America and Australia, which could be associated with the different treatment of

https://doi.org/10.5194/gmd-2023-4
Preprint. Discussion started: 9 March 2023

Geoscientific Model Development Discussions

MOPITT CO observations over ocean grids and the large differences in CO chemical sources and sinks. The updated model developed in this work is a useful extension of the adjoint of GEOS-Chem model.

1. Introduction

GEOS-Chem is a global 3D chemical transport model (CTM) and has been widely used to analyze the sources and variabilities of various atmospheric compositions (Li et al., 2019; Wang et al., 2019; Hammer et al., 2020; Jiang et al., 2022). GEOS-Chem model is driven by meteorological reanalysis data from the Goddard Earth Observing System (GEOS) of the Global Modeling and Assimilation Office (GMAO). Emissions in GEOS-Chem model are calculated based on the Harmonized Emissions Component (HEMCO) (Keller et al., 2014; Lin et al., 2021) with default support for state-of-the-art inventories such as CEDS (Community Emissions Data System) (Hoesly et al., 2018), MIX (Li et al., 2017) and NEI2011 (National Emissions Inventory). Based on GEOS-Chem forward model, the adjoint of the GEOS-Chem model (Henze et al., 2007) further provides the capability of backward simulation of physical and chemical processes within the 4D variational (4D-var) framework. The major advantage of the adjoint model is obtaining the sensitivity of atmospheric concentrations to multiple model variables within a single backward simulation. The major applications of the adjoint of GEOS-Chem model include inverse analyses of atmospheric pollutant emissions by minimizing the difference between simulations and observations (Jiang et al., 2017; Zhang et al., 2018; Qu et al., 2022) as well as sensitivity analyses to analyze the sources of atmospheric pollutants (Jiang et al., 2015; Zhao et al., 2019; Dedoussi et al., 2020).

The algorithm of the 4D-var framework requires identical model processes in the forward and backward simulations. Ideally, the code for the backward simulation should be updated following the GEOS-Chem forward code to take advantage of the new features in GEOS-Chem

https://doi.org/10.5194/gmd-2023-4
Preprint. Discussion started: 9 March 2023

forward simulations. However, the updates in the backward code are difficult and usually delayed. For example, the MEERA-2 meteorological reanalysis data with temporal coverage of 1979-present were supported in the GEOS-Chem forward simulations in v11-01. The adjoint of GEOS-Chem model does not support MERRA-2, and thus, long-term analysis must combine different meteorological reanalysis data, such as GEOS-4 (1985-2007), GEOS-5 (2004-2012) and GEOS-FP (2012-present), which can lead to discontinuity in the derived trends of emissions (Jiang et al., 2017). Furthermore, the HEMCO emission module was included in the GEOS-Chem forward simulations in v10-01. Adjoint of GEOS-Chem model does not support the HEMCO module, and thus, updated emission inventories such as CEDS, MIX and NEI2011 cannot be read conveniently, which can affect the performance in the simulated atmospheric compositions.

In this work, we develop the capability of the adjoint of GEOS-Chem model to support MERRA-2 meteorological data and HEMCO emission inventories. The results presented in this paper show the development, evaluation, and application of the developed capability to constrain carbon monoxide (CO) emissions by assimilating CO measurements from the Measurement of Pollution in the Troposphere (MOPITT). CO is one of the most important atmospheric pollutants and plays a key role in tropospheric chemistry. Sources of atmospheric CO include fossil fuel combustion, biomass burning and oxidation of hydrocarbons. The major sink of atmospheric CO is hydroxyl radical (OH). The simple chemical sink of atmospheric CO allows us to simulate atmospheric CO with linearized chemistry; for example, the tagged-CO mode of the GEOS-Chem model can reduce the calculation cost by 98% with respect to the full chemistry mode by reading archived monthly OH fields. The tagged-CO mode of the GEOS-Chem model has been widely used to investigate the sources and variabilities of atmospheric CO in recent decades (Heald et al., 2004; Kopacz et al., 2009; Jiang et al., 2017). The capability presented in this work is thus based on the tagged-CO mode, as it can effectively

https://doi.org/10.5194/gmd-2023-4
Preprint. Discussion started: 9 March 2023

accelerate the model development.

This paper is organized as follows: in Section 2, we describe the adjoint of GEOS-Chem model, the development of the new capability to support the MERRA-2 meteorological data and HEMCO emission inventories, and the MOPITT CO observations used in this work. In Section 3, we evaluated the performance of the developed model and presented an example application of 4D-var assimilation to constrain anthropogenic CO emissions in 2015 by assimilating MOPITT CO observations. Our conclusions follow in Section 4.

2. Methodology and Data

2.1 Adjoint of the GEOS-Chem model

We use version v35n of the adjoint of GEOS-Chem model. Our analysis is conducted at a horizontal resolution of 4°×5° with 47 vertical levels and employs the CO-only simulation (tagged-CO mode). The global default anthropogenic emission inventory in the standard version of the adjoint of GEOS-Chem model (hereafter referred to as GC-Adjoint-STD) is Global Emissions InitiAtive (GEIA), but is replaced by the following regional emission inventories: NEI2008 in North America, the Criteria Air Contaminants (CAC) inventory for Canada, the Big Bend Regional Aerosol and Visibility Observational (BRAVO) Study Emissions Inventory for Mexico (Kuhns et al., 2003), the Cooperative Program for Monitoring and Evaluation of the Long-range Transmission of Air Pollutants in Europe (EMEP) inventory for Europe in 2000 (Vestreng and Klein, 2002) and the INTEX-B Asia emissions inventory for 2006 (Zhang et al., 2009). Biomass burning emissions are based on the GFED3 (van der Werf et al., 2010).

The objective of the 4D-var approach is to minimize the difference between simulations and observations described by the cost function by adjusting the CO emissions iteratively (Henze et al., 2007):

https://doi.org/10.5194/gmd-2023-4
Preprint. Discussion started: 9 March 2023

Geoscientific Model Development Discussions
Open Access

$$J(x) = \sum_{i=1}^{N}[F_i(x) - z_i]^T S_\Sigma^{-1}[F_i(x) - z_i] + (x - x_a)^T S_a^{-1}(x - x_a) \quad (1)$$

where x is the state vector of CO emissions, N is the number of observations that are distributed in time over the assimilation period, z_i is a given measurement, and $F(x)$ is the forward model. The error estimates are assumed to be Gaussian and are given by S_Σ, the observational error covariance matrix, and S_a, the a priori error covariance matrix. We assume a uniform observation error of 20%. The combustion CO sources (fossil fuel, biofuel and biomass burning) and the oxidation source from biogenic volatile organic compound (VOC) are combined, assuming a 50% uniform a priori error. We optimize the source of CO from the oxidation of methane (CH_4) separately as an aggregated global source, assuming an a priori uncertainty of 25%. The CO emission estimates are optimized with monthly temporal resolution. We performed 40 iterations (forward + backward simulations) for each month, and the a posteriori CO emission estimates were calculated based on the last accepted iteration, which usually corresponded to the iteration with the lowest cost function.

2.2 Updates in emission inventories

A major objective of this work is to obtain consistent emissions between the adjoint of GEOS-Chem model and the GEOS-Chem forward model (v12-08-01, hereafter referred to as GC-v12). As shown in Fig. 1, we first initialize the array in [INITIAL] and batch read the emission data in [READ_DATA], which were interpolated offline with 1°×1° resolution by considering the mass conservation. Here, the data include the emission inventory data listed in Table S1 (see the SI), the corresponding scaling factor data and the mask map files of domain definitions. The data are scaled in [SCALE_DATA] by multiplying the corresponding annual, season, month, week, and 24-hour emission factors and are then online interpolated to the current resolution (4°×5° in this work) of the model by [RGRID_DATA], which was followed by the application of region masks in [MASK].

The emission variable of CO obtained in this part is written to the model memory in

https://doi.org/10.5194/gmd-2023-4
Preprint. Discussion started: 9 March 2023

emission.f and emission_adj.f. by calling DO_EMISSIONS. The GET_[TRACER] subroutines are used to obtain the CO emission variable, which participates in the calculation of physicochemical processes in the model, to interact with other modules. Finally, the variable is cleaned from the memory by the [CLEANUP] module. It should be noted that a two-step interpolation is employed in GC-Adjoint-HEMCO following GC-Adjoint-STD, for example, 0.1°×0.1° to 1°×1° and then to 4°×5° for the NEI2011 inventory, which is different from the one-step interpolation in GC-v12, for example, 0.1°×0.1° to 4°×5° directly for the NEI2011 inventory. The different interpolation methods can lead to differences in the interpolated emission data.

As shown in Table S1, the CEDS emission inventory (0.5°×0.5°) is adopted in GC-Adjoint-HEMCO to provide global default emissions for 1750-2019. The diurnal scale factors are applied to obtain CO emissions at different moments of the day. Fig. S1 (see the SI) shows CEDS CO emissions in 2015 in GC-v12 and GC-Adjoint-HEMCO and GEIA CO emissions in GC-Adjoint-STD, and we find noticeable differences in CO emissions between CEDS and GEIA. As shown in Table 1, the CEDS CO emissions in 2015 were 613.57 and 613.85 Tg/y in GC-v12 and GC-Adjoint-HEMCO, respectively, with a relative difference of 0.05% between GC-v12 and GC-Adjoint-HEMCO. The GEIA CO emissions in 2015 were 445.88 Tg/year in GC-Adjoint-STD.

The default CEDS inventory is replaced by the following regional emission inventories in GC-Adjoint-HEMCO: MIX in Asia (0.25°×0.25°), NEI2011 in the United States (0.1°×0.1°), DICE_AFRICA and EDGARV43 in Africa (0.1°×0.1°) and APEI in Canada (0.1°×0.1°). As shown in Fig. S2 (see the SI), the MIX inventory provides Asian emissions in 2008-2010, accompanied by diurnal scale factors to describe daily emission variation. The 1°×1° scale factors in the AnuualScalar.geos.1x1.nc file further provide the annual variation in 1985-2010. As shown in Table 1, the MIX CO emissions in 2015 were 321.18 and 321.71 Tg/y

https://doi.org/10.5194/gmd-2023-4
Preprint. Discussion started: 9 March 2023

Geoscientific Model Development Discussions

in GC-v12 and GC-Adjoint-HEMCO, respectively, with a relative difference of 0.17% between GC-v12 and GC-Adjoint-HEMCO. The INTEX-B CO emissions in 2015 were 353.03 Tg/y in GC-Adjoint-STD.

The NEI2011 inventory (Fig. S3, see the SI) provides anthropogenic emissions for the United States in 2011 with annual scalar factors from 2006-2013. The mid-week and weekend factors are read from NEI99.dow.geos.1x1.nc file since 1999 with all CO factors of 1.0 on weekdays and between 0.990 and 0.997 on Saturdays and Sundays. The NEI2011 CO emissions in 2015 were 35.83 and 37.70 Tg/y in GC-v12 and GC-Adjoint-HEMCO, respectively, with a relative difference of 5.22% between GC-v12 and GC-Adjoint-HEMCO. The NEI2008 CO emissions in 2015 were 52.87 Tg/y in GC-Adjoint-STD. APEI (Fig. S4, see the SI) is the primary source of anthropogenic emissions in the Canadian domain. The APEI CO emissions in 2015 were 6.10 and 6.17 Tg/y in GC-v12 and GC-Adjoint-HEMCO, respectively, with a relative difference of 1.14% between GC-v12 and GC-Adjoint-HEMCO. The CAC CO emissions in 2015 were 10.20 Tg/y in GC-Adjoint-STD. Following GC-v12, the CO emissions in APEI are enhanced by 19% to account for coemitted VOC in the tagged-CO simulation.

Emissions for the African domain are provided by the combination of DICE_AFRICA and EDGARV43 (Fig. S5, see the SI). Here DICE_AFRICA includes anthropogenic and biofuel emissions in 2013. We read the DICE_AFRICA emissions data into the model in two types according to the guidelines of the inventory. Emissions from sectors such as automobiles and motorcycles are aggregated into anthropogenic sources, and household-generated emissions such as charcoal and agricultural waste are aggregated into biofuel sources. Efficient combustion emissions from EDGAR v4.3 in 1970-2010 then compensate for the lacking sources in DICE_AFRICA. Daily variation factors for CO are also used here for emissions across the African region. The 2010 CO seasonal scale factors are used in EDGAR v4.3 for sectoral emission sources. The DICE_AFRICA and EDGARV43 CO emissions in 2015 were 83.42 and 83.02 Tg/y in GC-v12 and GC-Adjoint-HEMCO, respectively, with a relative difference of -0.48% between GC-v12 and GC-Adjoint-HEMCO. Following GC-v12, the CO emissions in DICE_AFRICA and EDGARV43 are enhanced by 19% to account for coemitted VOC in the tagged-CO simulation.

The biomass burning emission inventory in the GC-Adjoint-HEMCO is GFED4 (Fig. S6, see the SI), which includes dry matter emissions from a total of seven sectors in 1997-2019. The same GFED_emssion_factors.H header file as in the GC-v12 version is read in the GC-Adjoint-HEMCO. This file contains the ratio factors of atmospheric pollutants, and we multiply the ratio factors one by one according to the ID of each species to ensure that the species in the model have biomass burning sources. The GFED4 CO emissions in 2015 were 437.13 and 435.89 Tg/y in GC-v12 and GC-Adjoint-HEMCO, respectively, with a relative difference of -0.28% between GC-v12 and GC-Adjoint-HEMCO. The GFED3 CO emissions in 2015 were 382.04 Tg/year in GC-Adjoint-STD. Following GC-v12, the combustion CO sources in biomass burning are enhanced by 5% to consider the CO generated by VOC in the tagged-CO simulation.

Fig. 2 shows the total combustion CO emissions in 2015 from GC-v12, GC-Adjoint-HEMCO and GC-Adjoint-STD. As shown in Table 2, the regional combustion CO emissions are 320.66 and 320.38 Tg/y (Asia), 73.96 and 66.93 Tg/y (North America), 199.51 and 193.29/y Tg (Africa), 79.04 and 78.91 Tg/y (South America), 31.58 and 30.96 Tg/y (Europe) and 12.24 and 11.99 Tg/y (Australia) in GC-v12 and GC-Adjoint-HEMCO, respectively. Fig. 3 further shows the monthly combustion CO emissions in 2015 from GC-v12, GC-Adjoint-HEMCO and GC-Adjoint-STD, and there are good agreements in the monthly variation of CO emissions between GC-v12 and GC-Adjoint-HEMCO. The CO emissions in GC-Adjoint-STD are similar to those in GC-v12 and GC-Adjoint-HEMCO in winter and spring but with large differences in summer and autumn. This seasonal difference may reflect the influence of different emission inventories on biomass burning.

2.3 Updates in CO chemical sources and sinks

The biogenic emissions in GC-Adjoint-STD are Model of Emissions of Gases and Aerosols from Nature, version 2.0 (MEGANv2.0, Guenther et al. (2006)) in the full chemistry simulation but are GEIA in the tagged-CO simulation (Fig. S7, see the SI). Fisher et al. (2017) demonstrated improvement in modeled CO concentrations in tagged-CO simulation by reading archived VOC- and CH_4-generated CO fields provided by full chemistry simulation. The archived VOC- and CH_4-generated CO fields in 2013 (PCO_3Dglobal.geosfp.4x5.nc) were set as the default CO chemical sources in the tagged-CO simulation in GC-v12 and supported in GC-Adjoint-HEMCO. As shown in Table 2, the CO chemical sources (columns) obtained by reading the archived VOC- and CH_4-generated CO fields demonstrate good agreement between GC-v12 and GC-Adjoint-HEMCO. However, they are 30-60% lower than those in GEIA in GC-Adjoint-STD, and this difference could be partially associated with the inconsistency between the archived VOC-generated CO fields in 2013 and the actual meteorological data in 2015 in the simulation.

The default CH_4-generated CO emissions in GC-Adjoint-STD (Fig. S8, see the SI) are calculated based on averaged CH_4 concentrations in four latitude bands (90°S - 30°S, 30°S - 00°S, 00°N - 30°N, 30°N - 90°N), which are based on Climate Monitoring and Diagnostics Laboratory (CMDL) surface observations and Intergovernmental Panel on Climate Change (IPCC) future scenarios. As shown in Table 2, there are good agreements in the CH_4-generated CO emissions between GC-v12 and GC-Adjoint-HEMCO by reading PCO_3Dglobal.geosfp.4x5.nc, and they are 20-60% lower than those in CMDL/IPCC in GC-Adjoint-STD. Furthermore, the default archived monthly OH fields were updated following GC-v12 with updated calculations for the decay rate (KRATE, from JPL 03 to JPL 2006) in

GC-Adjoint-HEMCO. The subsequent CO sinks (Fig. S9, see the SI) in GC-v12 and GC-Adjoint-HEMCO are 20-40% higher than those in GC-Adjoint-STD.

2.4 Updates in meteorological data

The MERRA-2 meteorological data (1979-present) are supported in GC-Adjoint-HEMCO to ensure long-term consistency in the meteorological data in inverse analyses. The code porting to support MERRA-2 is more direct than emission inventories because the meteorological variables and vertical resolutions of MERRA-2 are the same as those of GEOS-FP (2012-present), while GEOS-FP is already supported by GC-Adjoint-STD. Fig. 4A-B show the averages of surface CO concentrations in 2015 from GC-Adjoint-HEMCO driven by MERRA-2 and GEOS-FP, respectively. Our results demonstrate lower surface CO concentrations driven by MERRA-2 (Fig. 4C), although there is good agreement in the spatial distributions of CO concentrations. Similarly, Fig. 4D-F show the averages of CO columns in 2015 from GC-Adjoint-HEMCO driven by MERRA-2 and GEOS-FP and their differences. Despite the noticeable differences in surface CO concentrations (Fig. 4C), the differences in CO columns (Fig. 4F) are much smaller, and the modeled CO columns driven by MERRA-2 are higher than those driven by GEOS-FP over the Indian Ocean. The discrepancy between surface and column CO in Fig. 4 may reflect the impacts of different convective transports on the modeled CO concentrations.

2.5 MOPITT CO measurements

The MOPITT data used here were obtained from the joint retrieval (V7J) of CO from thermal infrared (TIR, 4.7μm) and near-infrared (NIR, 2.3μm) radiances using an optimal estimation approach (Worden et al., 2010; Deeter et al., 2017). The retrieved volume mixing ratios (VMR) are reported as layer averages of 10 pressure levels with a footprint of 22 km × 22 km. Following Jiang et al. (2017), we reject MOPITT data with CO column amounts less than 5×10^{17} molec/cm^2 and with low cloud observations. Since the NIR channel measures

https://doi.org/10.5194/gmd-2023-4
Preprint. Discussion started: 9 March 2023

reflected solar radiation, only daytime data are considered.

3. Model evaluation and application

3.1 CO concentrations in the forward simulations

We first evaluate the performance of GC-Adjoint-HEMCO in forward simulations. Fig. 5 shows the averages of surface and column CO concentrations in 2015 from GC-v12, GC-Adjoint-HEMCO and GC-Adjoint-STD. As shown in Table 2, the regional differences between GC-v12 and GC-Adjoint-HEMCO are 2.6%, -5.7%, -4.6%, -1.7%, -1.4% and -3.6% in surface CO concentrations, and -2.3%, -3.6%, -3.3%, -3.1%, -3.3% and -4.1% in CO columns over Asia, North America, Africa, South America, Europe, and Australia, respectively. The differences in CO concentrations between GC-v12 and GC-Adjoint-HEMCO are expected in view of the comparable differences in regional emissions, chemical sources and sinks, as shown in Table 2. The regional differences in CO concentrations between GC-v12 and GC-Adjoint-STD are larger: 4.6%, -10.1%, 6.3%, 22.5%, 6.4% and 25.7% in surface CO concentrations, and -0.7%, -9.9%, 2.5%, 8.0%, -5.8% and 8.5% in CO columns over Asia, North America, Africa, South America, Europe, and Australia, respectively.

3.2 Observing system simulation experiments with pseudo-CO observations

Here we further evaluate the performance of GC-Adjoint-HEMCO as a 4D-var framework using observing system simulation experiments (OSSE). OSSE is a useful method and has been widely used to evaluate the performance of various data assimilation systems (Jones et al., 2003; Barré et al., 2015; Shu et al., 2022). In contrast to assimilations by assimilating actual atmospheric observations, pseudo-observations are usually generated by model simulations and then assimilated in OSSE. The true atmospheric states are known in OSSEs as they are used to produce the pseudo-observations, and consequently, the difference between assimilated and true atmospheric states describes the capability of the assimilation

https://doi.org/10.5194/gmd-2023-4
Preprint. Discussion started: 9 March 2023

systems to converge to the true atmospheric states in assimilations when assimilating actual observations.

The pseudo-observations in this work are produced by archiving CO concentrations from GC-Adjoint-HEMCO forward simulations with the CO emissions unchanged (i.e., the default CO emission inventory such as CEDS, MIX and NEI2011). According to the usage of pseudo-observations, two types of OSSE are performed in this work: 1) full modeled CO fields are assimilated as pseudo-observations so that we have pseudo-CO observations at every grid/level and time step (hereafter referred to as OSSE-FullOBS). This experiment is designed to evaluate the performance of the assimilation system under ideal conditions with full coverage of observations. 2) The modeled CO fields are sampled at the locations/times of MOPITT CO observations and smoothed with MOPITT a priori concentrations and averaging kernels to produce MOPITT-like pseudo-CO observations (hereafter referred to as OSSE-MOPITT). This experiment is designed to evaluate the performance of the assimilation system under actual conditions with limited coverage of observations.

In the inverse analysis with the pseudo-CO observations, we reduce the anthropogenic CO emissions by 50% so that the objective of the OSSE is to produce scaling factors that can return the source estimate to the default emissions (i.e., scaling factors of 1.0). Fig. 6A shows the annual scaling factors in 2015 in OSSE-FullOBS. After 40 iterations, the a posteriori anthropogenic CO emission estimates converge to the true states in all major emission regions. As shown in Table 3, the regional scaling factors of OSSE-FullOBS are 1.00, 0.97, 0.97, 1.00, 0.98 and 0.94 for anthropogenic CO emissions over Asia, North America, Africa, South America, Europe, and Australia, respectively.

Furthermore, Fig. 6D shows the annual scaling factors in OSSE-MOPITT, which are noticeably worse than those in Fig. 6A. The regional scaling factors of OSSE-MOPITT are 1.04, 0.88, 1.01, 1.02, 0.84 and 0.81 for anthropogenic CO emissions over Asia, North

https://doi.org/10.5194/gmd-2023-4
Preprint. Discussion started: 9 March 2023

America, Africa, South America, Europe, and Australia, respectively. With respect to OSSE-FullOBS, the limited coverage of observations in OSSE-MOPITT has resulted in approximately 15% underestimations in the a posteriori CO emission estimates over North America and Europe. In addition, Fig. 6B-C and Fig. 6E-F show the a priori and a posteriori biases in the modeled CO columns. We find dramatic improvements in the modeled CO columns, which confirms the reliability of the 4D-var assimilation system. The difference between Fig. 6B and 6E reflects the influence of the application of MOPITT averaging kernels, which lead to larger negative biases in the a priori simulation. It should be noted that we cannot expect comparable improvement in the actual assimilations because of the potential effects of model and observation errors.

3.3 Anthropogenic CO emissions constrained with MOPITT CO observations

As an example of the application of GC-Adjoint-HEMCO, here we constrain anthropogenic CO emissions in 2015 by assimilating MOPITT CO observations. Fig.7A shows the relative differences between modeled and MOPITT CO columns at the beginning of each month in 2015 (i.e., biases in monthly initial CO conditions) in the original GEOS-Chem simulations. We find dramatic underestimations in the modeled CO columns by approximately 30-40%. As indicated by previous studies (Jiang et al., 2013; Jiang et al., 2017), the biases in monthly initial CO conditions are caused by model biases in CO concentrations accumulated in previous months. A lack of consideration of the model biases, as shown in Fig. 7A, can result in overestimations in the derived monthly CO emission estimates.

Following Jiang et al. (2017), a suboptimal sequential Kalman filter (Todling and Cohn, 1994; Tang et al., 2022) was employed in this work to optimize the modeled CO concentrations with an hourly resolution by combining GC-Adjoint-HEMCO forward simulation and MOPITT CO observations. The CO concentrations provided by the Kalman filter assimilations were archived at the beginning of each month, which were used as the optimized monthly initial

https://doi.org/10.5194/gmd-2023-4
Preprint. Discussion started: 9 March 2023

CO conditions in the inverse analysis. As shown in Fig. 7B, the biases in the modeled CO columns in the optimized initial CO conditions are pronounced lower than those in the original simulation (Fig. 7A). The optimization of the initial CO conditions is essential for our inverse analysis, as it can ensure that the adjustments in CO emissions are dominated by the differences between simulations and observations in the current month instead of the 30-40% underestimations in CO columns accumulated in previous months.

Fig. 8A shows the distribution of a priori anthropogenic CO emissions in 2015. The regional a priori anthropogenic CO emissions (as shown in Table 4) are 243.53, 34.42, 23.24, 30.39, 25.94 and 2.02 Tg/y over Asia, North America, Africa, South America, Europe, and Australia, respectively. As shown in Fig. 8B, our inverse analysis suggests a wide distribution of underestimations in the a priori anthropogenic CO emissions in 2015 except in E. China. The regional scaling factors (Table 4) are 1.16, 1.47, 1.52, 1.41, 1.60 and 1.38, and the a posteriori anthropogenic CO emissions are 283.20, 50.47, 35.34, 42.92, 41.62 and 2.79 Tg/y over Asia, North America, Africa, South America, Europe, and Australia, respectively. As shown in Fig. 8C, we find noticeable underestimations in the modeled CO columns in the a priori simulations, despite the negative biases being much weaker than those in Fig. 7A due to the optimization of the initial CO conditions. The negative biases are effectively reduced in the a posteriori simulation driven by the a posteriori CO emission estimates (Fig. 8D).

Finally, we compare the a posteriori CO emission estimates in this work with Jiang et al. (2017), who constrained CO emissions in 2001-2015 with GC-Adjoint-STD by assimilating the same MOPITT CO observations. As shown in Table 4, the a posteriori anthropogenic CO emission estimates in this work match well with Jiang et al. (2017) in North America and Africa but are 38%, 157% and 228% higher than those in Jiang et al. (2017) in Asia, South America and Australia, respectively. A major discrepancy between this work and Jiang et al. (2017) is the treatment of ocean grids. Jiang et al. (2017) defined ocean grids as continental boundary

https://doi.org/10.5194/gmd-2023-4
Preprint. Discussion started: 9 March 2023

conditions, which were rewritten hourly using the optimized CO concentrations archived from the suboptimal sequential Kalman filter by assimilating MOPITT CO observations. Only MOPITT data over land were assimilated in the 4D-var assimilations in Jiang et al. (2017) without any change in CO distribution over the ocean. In addition, the large differences in chemical sources and sinks between GC-Adjoint-HEMCO and GC-Adjoint-STD, for example, lower VOC-generated CO emissions by 40-60% and higher CO sinks by 20-40% in GC-Adjoint-HEMCO as shown in Table 2, may also contribute to the discrepancy in the derived a posteriori CO emission estimates.

As shown in Fig. 8D, the a posteriori simulation demonstrates positive biases in CO columns over China and Southeast Asia, which is a signal of overestimated local CO emissions; meanwhile, the negative biases over the northern Pacific Ocean are reduced in the a posteriori simulation. The negative biases over the remote ocean are more affected by CO chemical sources and sinks; however, biases in chemical sources cannot be effectively adjusted because of the global uniform scaling factor for CH_4-generated CO emissions; biases in chemical sinks cannot be adjusted because of the fixed OH fields in the tagged-CO simulation. Jiang et al. (2017) tried to address this problem by defining continental boundary conditions so that the inverse analysis is dominated by local MOPITT observations to avoid the influence of model biases accumulated within the long-range transport. Conversely, CO emissions over China and Southeast Asia are overestimated in this work to offset the negative biases over the northern Pacific Ocean. We expect similar overestimations in the a posteriori CO emission estimates over South America, southern Africa, and Australia in this work because it is the effective pathway to reduce the negative bias over the ocean in the Southern Hemisphere.

4. Conclusion

An updated version (GC-Adjoint-HEMCO) of the adjoint of GEOS-Chem model was developed in this work. The major updates of GC-Adjoint-HEMCO include 1) support for the

MERRA-2 meteorological data so that we can perform long-term inverse analysis with consistent meteorological data in 1979-present and 2) support for the HEMCO including emission inventories CEDS, MIX, NEI2011, DICE_AF, AF_EDGAR43, APEI and GFED4. The updated emission inventories are critical for reliable inverse analysis, as they are helpful for better convergence of 4D-var assimilations by setting the more reasonable a priori penalty in the cost function. CO emissions from various inventories, chemical sources and sinks, and surface and column CO concentrations provided by GC-Adjoint-HEMCO are compared with those provided by GC-v12 and GC-Adjoint-STD, and we find good agreement in the forward simulations between GC-Adjoint-HEMCO and GC-v12.

Two types of OSSE are employed to evaluate the performance of GC-Adjoint-HEMCO in 4D-var assimilations. The a posteriori CO emissions converge to the true states in all major emission regions with fully covered pseudo-CO observations; the limited coverage of observations by sampling the pseudo-CO observations at the locations/times of MOPITT CO observations and smoothing with MOPITT averaging kernels resulted in approximately 15% underestimations in the a posteriori CO emissions over North America and Europe. Furthermore, as an example application of GC-Adjoint-HEMCO, we constrain anthropogenic CO emissions in 2015 by assimilating MOPITT CO observations. The a posteriori anthropogenic CO emission estimates derived in this work match well with Jiang et al. (2017) in North America and Africa but are overestimated in Asia, South America and Australia, which could be associated with the different treatment of MOPITT CO observations over ocean grids and the large differences in CO chemical sources and sinks. The GC-Adjoint-HEMCO developed in this work is a useful extension for the adjoint of GEOS-Chem model. More efforts are needed to support tagged-CO simulation with higher spatial resolutions and to support full chemistry simulation in GC-Adjoint-HEMCO.

Code and data availability: The MOPITT CO data can be downloaded from https://asdc.larc.nasa.gov/data/MOPITT/. The GEOS-Chem model (version 12.8.1) can be downloaded from http://wiki.seas.harvard.edu/geos-chem/index.php/GEOS-Chem_12#12.8.1. The adjoint of GEOS-Chem model (GC-Adjoint-STD) can be downloaded from http://wiki.seas.harvard.edu/geos-chem/index.php/GEOS-Chem_Adjoint. The adjoint of GEOS-Chem model (GC-Adjoint-HEMCO) can be downloaded from https://doi.org/10.5281/zenodo.7512111.

Author Contributions: Z.J. designed the research. Z.T. developed the model code and performed the research. Z.J. and Z.T. wrote the manuscript. All authors contributed to discussions and editing the manuscript.

Competing interests: The authors declare that they have no conflicts of interest.

Acknowledgments: We thank the providers of the MOPITT CO data. The numerical calculations in this paper have been done on the supercomputing system in the Supercomputing Center of University of Science and Technology of China. This work was supported by the Hundred Talents Program of Chinese Academy of Science and National Natural Science Foundation of China (42277082, 41721002).

Tables and Figures

Table 1. CO emissions for each inventory in 2015 with unit Tg/y.

Table 2. Regional combustion CO emissions, VOC-generated CO (PCO_NMVOC), CH_4-generated CO (PCO_CH_4), CO sinks (CO_OH, calculated as CO_OH = KRATE×CO×OH), and simulated surface and column CO concentrations in 2015. The region definitions are shown in Fig. 2A.

https://doi.org/10.5194/gmd-2023-4
Preprint. Discussion started: 9 March 2023

Table 3. Annual scaling factors of anthropogenic CO emissions in OSSEs. The scaling factors represent the ratio of the estimated to true emissions. The ratio for the first guess is 0.5. The actual value is 1.0. The pseudo-observations are produced by GC-Adjoint-HEMCO forward simulation. The full modeled CO fields are used in OSSE-FullOBS as pseudo-CO observations. The modeled CO fields are smoothed with MOPITT averaging kernels to produce MOPITT-like pseudo-CO observations in OSSE-MOPITT.

Table 4. Regional anthropogenic CO emissions (with unit Tg/y) and annual scaling factors in 2015 in this work and Jiang et al. 2017.

Fig. 1. Framework to read the updated emission inventories in GC-Adjoint-HEMCO.

Fig. 2. Total combustion CO emissions in 2015 from (a) GC-v12; (b) GC-Adjoint-HEMCO; (c) GC-Adjoint-STD. The unit is molec/cm^2/s.

Fig. 3. Monthly variation in combustion CO emissions in 2015 from GC-v12, GC-Adjoint-HEMCO and GC-Adjoint-STD.

Fig. 4. Averages of surface CO concentrations in 2015 from (a) GC-Adjoint-HEMCO driven by MERRA-2, (b) GC-Adjoint-HEMCO driven by GEOS-FP and (c) their difference; (d-f) same as panels a-c, but for CO columns.

Fig. 5. Averages of surface CO concentrations in 2015 from (a) GC-v12; (b) GC-Adjoint-HEMCO; (c) GC-Adjoint-STD. (d-f) same as panels a-c, but for CO columns.

Fig. 6. (a) Annual scaling factors in OSSE-FullOBS. The scaling factors represent the ratio of the estimated to true emissions. The ratio for the first guess is 0.5. The actual value is 1.0. (b-c) the a priori and a posteriori biases calculated by (model-observation)/observation in OSSE-Full. (d-f) same as panels a-c, but for OSSE-MOPITT.

Fig. 7. (a) Biases in monthly initial CO conditions in 2015 in the original GEOS-Chem simulation. (b) same as panel a, but with optimized initial CO conditions provided by suboptimal sequential Kalman filter. The biases are calculated by (model-MOPITT)/MOPITT.

https://doi.org/10.5194/gmd-2023-4
Preprint. Discussion started: 9 March 2023

Fig. 8. (a) A priori anthropogenic CO emissions in 2015 with unit molec/cm^2/s; (b) Annual scaling factors for CO emissions in 2015. The scaling factors represent the ratio of the estimated to true emissions. (c-d) the a priori and a posteriori biases calculated by (model-MOPITT)/MOPITT.

References

Barré, J., Edwards, D., Worden, H., Da Silva, A., and Lahoz, W.: On the feasibility of monitoring carbon monoxide in the lower troposphere from a constellation of Northern Hemisphere geostationary satellites. (Part 1), Atmos Environ, 113, 63-77, 10.1016/j.atmosenv.2015.04.069, 2015.

Dedoussi, I. C., Eastham, S. D., Monier, E., and Barrett, S. R. H.: Premature mortality related to United States cross-state air pollution, Nature, 578, 261-265, 10.1038/s41586-020-1983-8, 2020.

Deeter, M. N., Edwards, D. P., Francis, G. L., Gille, J. C., Martínez-Alonso, S., Worden, H. M., and Sweeney, C.: A climate-scale satellite record for carbon monoxide: the MOPITT Version 7 product, Atmos Meas Tech, 10, 2533-2555, 10.5194/amt-10-2533-2017, 2017.

Fisher, J. A., Murray, L. T., Jones, D. B. A., and Deutscher, N. M.: Improved method for linear carbon monoxide simulation and source attribution in atmospheric chemistry models illustrated using GEOS-Chem v9, Geosci Model Dev, 10, 4129-4144, 10.5194/gmd-10-4129-2017, 2017.

Guenther, A., Karl, T., Harley, P., Wiedinmyer, C., Palmer, P. I., and Geron, C.: Estimates of global terrestrial isoprene emissions using MEGAN (Model of Emissions of Gases and Aerosols from Nature), Atmos Chem Phys, 6, 3181-3210, 10.5194/acp-6-3181-2006, 2006.

Hammer, M. S., van Donkelaar, A., Li, C., Lyapustin, A., Sayer, A. M., Hsu, N. C., Levy, R. C., Garay, M. J., Kalashnikova, O. V., Kahn, R. A., Brauer, M., Apte, J. S., Henze, D. K., Zhang, L., Zhang, Q., Ford, B., Pierce, J. R., and Martin, R. V.: Global Estimates and Long-Term Trends of Fine Particulate Matter Concentrations (1998-2018), Environ Sci Technol, 54, 7879-7890, 10.1021/acs.est.0c01764, 2020.

Heald, C. L., Jacob, D. J., Jones, D. B. A., Palmer, P. I., Logan, J. A., Streets, D. G., Sachse, G. W., Gille, J. C., Hoffman, R. N., and Nehrkorn, T.: Comparative inverse analysis of satellite (MOPITT) and aircraft (TRACE-P) observations to estimate Asian sources of carbon monoxide, J Geophys Res-Atmos, 109, D23306, 10.1029/2004jd005185, 2004.

Henze, D. K., Hakami, A., and Seinfeld, J. H.: Development of the adjoint of GEOS-Chem, Atmos Chem Phys, 7, 2413-2433, 10.5194/acp-7-2413-2007, 2007.

Hoesly, R. M., Smith, S. J., Feng, L., Klimont, Z., Janssens-Maenhout, G., Pitkanen, T., Seibert, J. J., Vu, L., Andres, R. J., Bolt, R. M., Bond, T. C., Dawidowski, L., Kholod, N., Kurokawa, J.-i., Li, M., Liu, L., Lu, Z., Moura, M. C. P., O'Rourke, P. R., and Zhang, Q.: Historical (1750–2014) anthropogenic emissions of reactive gases and aerosols from the

Community Emissions Data System (CEDS), Geosci Model Dev, 11, 369-408, 10.5194/gmd-11-369-2018, 2018.

Jiang, Z., Jones, D. B. A., Worden, H. M., Deeter, M. N., Henze, D. K., Worden, J., Bowman, K. W., Brenninkmeijer, C. A. M., and Schuck, T. J.: Impact of model errors in convective transport on CO source estimates inferred from MOPITT CO retrievals, J Geophys Res-Atmos, 118, 2073-2083, 10.1002/jgrd.50216, 2013.

Jiang, Z., Worden, J. R., Jones, D. B. A., Lin, J. T., Verstraeten, W. W., and Henze, D. K.: Constraints on Asian ozone using Aura TES, OMI and Terra MOPITT, Atmos Chem Phys, 15, 99-112, 10.5194/acp-15-99-2015, 2015.

Jiang, Z., Worden, J. R., Worden, H., Deeter, M., Jones, D. B. A., Arellano, A. F., and Henze, D. K.: A 15-year record of CO emissions constrained by MOPITT CO observations, Atmos Chem Phys, 17, 4565-4583, 10.5194/acp-17-4565-2017, 2017.

Jiang, Z., Zhu, R., Miyazaki, K., McDonald, B. C., Klimont, Z., Zheng, B., Boersma, K. F., Zhang, Q., Worden, H., Worden, J. R., Henze, D. K., Jones, D. B. A., Denier van der Gon, H. A. C., and Eskes, H.: Decadal Variabilities in Tropospheric Nitrogen Oxides Over United States, Europe, and China, J Geophys Res-Atmos, 127, e2021JD035872, 10.1029/2021jd035872, 2022.

Jones, D. B. A., Bowman, K. W., Palmer, P. I., Worden, J. R., Jacob, D. J., Hoffman, R. N., Bey, I., and Yantosca, R. M.: Potential of observations from the Tropospheric Emission Spectrometer to constrain continental sources of carbon monoxide, J Geophys Res-Atmos, 108, 2003JD003702, 10.1029/2003jd003702, 2003.

Keller, C. A., Long, M. S., Yantosca, R. M., Da Silva, A. M., Pawson, S., and Jacob, D. J.: HEMCO v1.0: a versatile, ESMF-compliant component for calculating emissions in atmospheric models, Geosci Model Dev, 7, 1409-1417, 10.5194/gmd-7-1409-2014, 2014.

Kopacz, M., Jacob, D. J., Henze, D. K., Heald, C. L., Streets, D. G., and Zhang, Q.: Comparison of adjoint and analytical Bayesian inversion methods for constraining Asian sources of carbon monoxide using satellite (MOPITT) measurements of CO columns, Journal of Geophysical Research, 114, D04305, 10.1029/2007jd009264, 2009.

Kuhns, H., Green, M., and Etyemezian, V.: Big Bend Regional Aerosol and Visibility Observational (BRAVO) Study Emissions Inventory, Report prepared for BRAVO Steering Committee, Desert Research Institute, Las Vegas, Nevada, 2003.

Li, K., Jacob, D. J., Liao, H., Shen, L., Zhang, Q., and Bates, K. H.: Anthropogenic drivers of 2013-2017 trends in summer surface ozone in China, Proc Natl Acad Sci USA, 116, 422-427, 10.1073/pnas.1812168116, 2019.

Li, M., Zhang, Q., Kurokawa, J.-i., Woo, J.-H., He, K., Lu, Z., Ohara, T., Song, Y., Streets, D. G., Carmichael, G. R., Cheng, Y., Hong, C., Huo, H., Jiang, X., Kang, S., Liu, F., Su, H., and Zheng, B.: MIX: a mosaic Asian anthropogenic emission inventory under the international collaboration framework of the MICS-Asia and HTAP, Atmos Chem Phys, 17, 935-963, 10.5194/acp-17-935-2017, 2017.

Lin, H., Jacob, D. J., Lundgren, E. W., Sulprizio, M. P., Keller, C. A., Fritz, T. M., Eastham, S. D., Emmons, L. K., Campbell, P. C., Baker, B., Saylor, R. D., and Montuoro, R.: Harmonized Emissions Component (HEMCO) 3.0 as a versatile emissions component for

https://doi.org/10.5194/gmd-2023-4
Preprint. Discussion started: 9 March 2023

atmospheric models: application in the GEOS-Chem, NASA GEOS, WRF-GC, CESM2, NOAA GEFS-Aerosol, and NOAA UFS models, Geosci Model Dev, 14, 5487-5506, 10.5194/gmd-14-5487-2021, 2021.

Qu, Z., Henze, D. K., Worden, H. M., Jiang, Z., Gaubert, B., Theys, N., and Wang, W.: Sector‐Based Top‐Down Estimates of NO_x, SO_2, and CO Emissions in East Asia, Geophys Res Lett, 49, e2021GL096009, 10.1029/2021gl096009, 2022.

Shu, L., Zhu, L., Bak, J., Zoogman, P., Han, H., Long, X., Bai, B., Liu, S., Wang, D., Sun, W., Pu, D., Chen, Y., Li, X., Sun, S., Li, J., Zuo, X., Yang, X., and Fu, T.-M.: Improved ozone simulation in East Asia via assimilating observations from the first geostationary air-quality monitoring satellite: Insights from an Observing System Simulation Experiment, Atmos Environ, 274, 119003, 10.1016/j.atmosenv.2022.119003, 2022.

Tang, Z., Chen, J., and Jiang, Z.: Discrepancy in assimilated atmospheric CO over East Asia in 2015–2020 by assimilating satellite and surface CO measurements, Atmos Chem Phys, 22, 7815-7826, 10.5194/acp-22-7815-2022, 2022.

Todling, R., and Cohn, S. E.: Suboptimal schemes for atmospheric data assimilation based on the Kalman filter, Monthly Weather Review, 122, 10.1175/1520-0493(1994)122<2530:SSFADA>2.0.CO;2, 1994.

van der Werf, G. R., Randerson, J. T., Giglio, L., Collatz, G. J., Mu, M., Kasibhatla, P. S., Morton, D. C., DeFries, R. S., Jin, Y., and van Leeuwen, T. T.: Global fire emissions and the contribution of deforestation, savanna, forest, agricultural, and peat fires (1997–2009), Atmos Chem Phys, 10, 11707-11735, 10.5194/acp-10-11707-2010, 2010.

Vestreng, V., and Klein, H.: Emission data reported to UNECE/EMEP. Quality assurance and trend analysis and Presentation of WebDab, Norwegian Meteorological Institute, Oslo, Norway, 2002.

Wang, X., Jacob, D. J., Eastham, S. D., Sulprizio, M. P., Zhu, L., Chen, Q., Alexander, B., Sherwen, T., Evans, M. J., Lee, B. H., Haskins, J. D., Lopez-Hilfiker, F. D., Thornton, J. A., Huey, G. L., and Liao, H.: The role of chlorine in global tropospheric chemistry, Atmos Chem Phys, 19, 3981-4003, 10.5194/acp-19-3981-2019, 2019.

Worden, H. M., Deeter, M. N., Edwards, D. P., Gille, J. C., Drummond, J. R., and Nédélec, P.: Observations of near-surface carbon monoxide from space using MOPITT multispectral retrievals, Journal of Geophysical Research, 115, D18314, 10.1029/2010jd014242, 2010.

Zhang, L., Chen, Y., Zhao, Y., Henze, D. K., Zhu, L., Song, Y., Paulot, F., Liu, X., Pan, Y., Lin, Y., and Huang, B.: Agricultural ammonia emissions in China: reconciling bottom-up and top-down estimates, Atmos Chem Phys, 18, 339-355, 10.5194/acp-18-339-2018, 2018.

Zhang, Q., Streets, D. G., Carmichael, G. R., He, K. B., Huo, H., Kannari, A., Klimont, Z., Park, I. S., Reddy, S., Fu, J. S., Chen, D., Duan, L., Lei, Y., Wang, L. T., and Yao, Z. L.: Asian emissions in 2006 for the NASA INTEX-B mission, Atmos Chem Phys, 9, 5131-5153, 10.5194/acp-9-5131-2009, 2009.

Zhao, H., Geng, G., Zhang, Q., Davis, S. J., Li, X., Liu, Y., Peng, L., Li, M., Zheng, B., Huo, H., Zhang, L., Henze, D. K., Mi, Z., Liu, Z., Guan, D., and He, K.: Inequality of household consumption and air pollution-related deaths in China, Nat Commun, 10, 4337, 10.1038/s41467-019-12254-x, 2019.

https://doi.org/10.5194/gmd-2023-4
Preprint. Discussion started: 9 March 2023

Geoscientific Model Development
Discussions

Inventories	GC-v12	GC-Adjoint-HEMCO	Inventories	GC-Adjoint-STD
CEDS	613.57	613.85	GEIA	445.88
MIX	321.18	321.71	INTEX-B	353.03
NEI2011	35.83	37.70	NEI2008	52.87
DICE_AF + AF_EDGAR43	83.42	83.02	\	\
APEI	6.10	6.17	CAC	10.20
GFED4	437.13	435.89	GFED3	382.04

Table 1. CO emissions for each inventory in 2015 with unit Tg/y.

	Combustion Emission (Tg/y)			PCO_NMVOC (kg/s)			PCO_CH4 (kg/s)		
Region \ Version	GC-v12	GC-Adjoint-HEMCO	GC-Adjoint-STD	GC-v12	GC-Adjoint-HEMCO	GC-Adjoint-STD	GC-v12	GC-Adjoint-HEMCO	GC-Adjoint-STD
Asia	320.66	320.38	331.65	15.49	15.52	22.37	14.21	14.40	10.67
North America	73.96	66.93	60.65	7.05	6.83	14.75	7.45	7.66	5.23
Africa	199.51	193.29	179.22	34.57	33.92	52.38	19.57	19.85	16.18
South America	79.04	78.91	75.82	44.15	42.55	74.64	17.14	17.42	14.08
Europe	31.58	30.96	48.48	4.20	4.14	10.17	7.13	7.41	4.58
Australia	12.24	11.99	22.87	21.23	20.68	48.89	13.88	14.62	10.67
	CO_OH (kg/s)			CO (surface ppbv)			CO (column xco)		
Region \ Version	GC-v12	GC-Adjoint-HEMCO	GC-Adjoint-STD	GC-v12	GC-Adjoint-HEMCO	GC-Adjoint-STD	GC-v12	GC-Adjoint-HEMCO	GC-Adjoint-STD
Asia	52.26	51.34	40.87	179.56	184.29	187.90	90.23	88.16	89.58
North America	23.02	22.57	16.20	120.38	113.49	108.27	79.16	76.27	71.35
Africa	63.78	61.84	51.03	133.56	127.38	141.97	84.26	81.52	86.36
South America	49.06	48.85	41.25	107.98	106.16	132.24	72.93	70.67	78.75
Europe	20.65	20.92	14.27	112.88	111.33	120.09	74.83	72.34	70.45
Australia	31.42	31.98	25.27	67.45	65.00	84.80	56.35	54.02	61.15

Table 2. Regional combustion CO emissions, VOC-generated CO (PCO_NMVOC), CH_4-generated CO (PCO_CH_4), CO sinks (CO_OH, calculated as CO_OH = KRATE×CO×OH), and simulated surface and column CO concentrations in 2015. The region definitions are shown in Fig. 2A.

https://doi.org/10.5194/gmd-2023-4
Preprint. Discussion started: 9 March 2023

	Scaling Factors OSSE-FullOBS	Scaling Factors OSSE-MOPITT
Asia	**1.00**	**1.04**
North America	**0.97**	**0.88**
Africa	**0.97**	**1.01**
South America	**1.00**	**1.02**
Europe	**0.98**	**0.84**
Australia	**0.94**	**0.81**

Table 3. Annual scaling factors of anthropogenic CO emissions in OSSEs. The scaling factors represent the ratio of the estimated to true emissions. The ratio for the first guess is 0.5. The actual value is 1.0. The pseudo-observations are produced by GC-Adjoint-HEMCO forward simulation. The full modeled CO fields are used in OSSE-FullOBS as pseudo-CO observations. The modeled CO fields are smoothed with MOPITT averaging kernels to produce MOPITT-like pseudo-CO observations in OSSE-MOPITT.

		Asia	North America	Africa	South America	Europe	Australia
This work	**A priori CO emissions**	**243.53**	**34.42**	**23.24**	**30.39**	**25.94**	**2.02**
	A posteriori CO emissions	**283.20**	**50.47**	**35.34**	**42.92**	**41.62**	**2.79**
	Scaling Factors	**1.16**	**1.47**	**1.52**	**1.41**	**1.60**	**1.38**
Jiang et al. 2017	**A priori CO emissions**	**270.50**	**43.70**	**29.39**	**17.47**	**44.45**	**0.83**
	A posteriori CO emissions	**205.40**	**47.06**	**35.04**	**16.67**	**53.58**	**0.82**
	Scaling Factors	**0.76**	**1.08**	**1.19**	**0.95**	**1.21**	**0.99**

Table 4. Regional anthropogenic CO emissions (with unit Tg/y) and annual scaling factors in 2015 in this work and Jiang et al. 2017.

https://doi.org/10.5194/gmd-2023-4
Preprint. Discussion started: 9 March 2023

Geoscientific Model Development
Discussions
Open Access

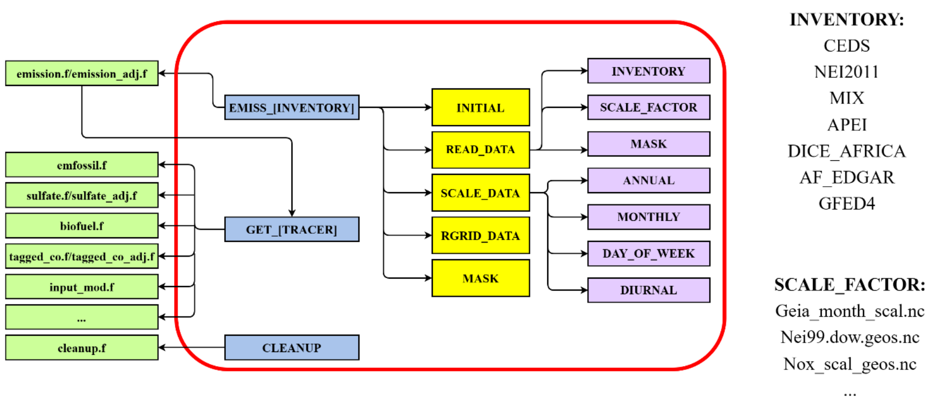

Fig. 1. Framework to read the updated emission inventories in GC-Adjoint-HEMCO.

https://doi.org/10.5194/gmd-2023-4
Preprint. Discussion started: 9 March 2023

Geoscientific Model Development
Discussions
Open Access

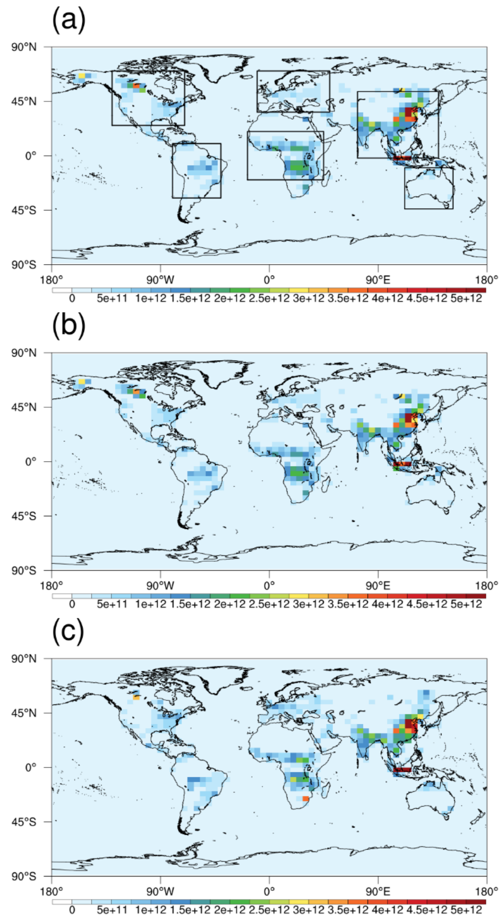

Fig. 2. Total combustion CO emissions in 2015 from (a) GC-v12; (b) GC-Adjoint-HEMCO; (c) GC-Adjoint-STD. The unit is molec/cm^2/s.

https://doi.org/10.5194/gmd-2023-4
Preprint. Discussion started: 9 March 2023

Geoscientific Model Development
Discussions

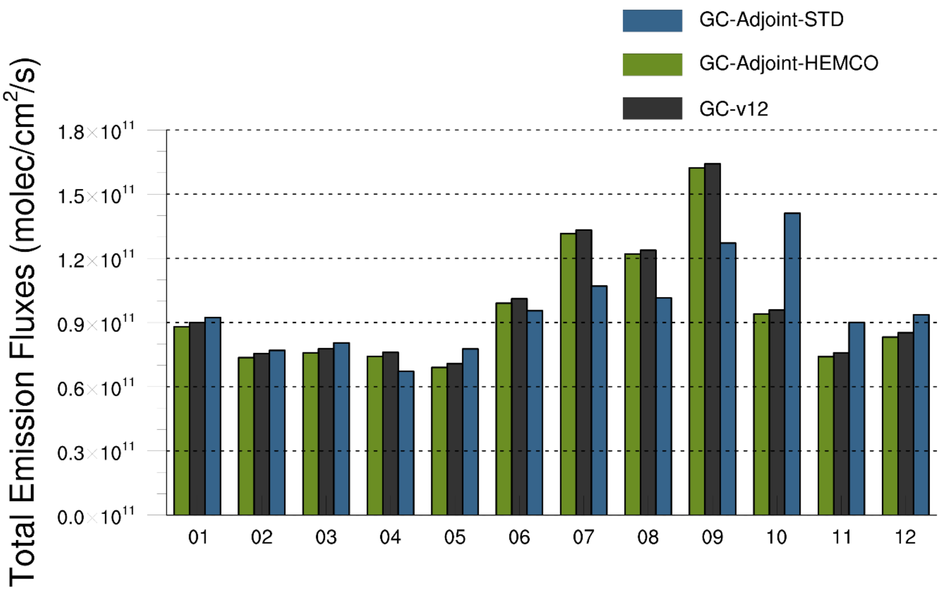

Fig. 3. Monthly variation in combustion CO emissions in 2015 from GC-v12, GC-Adjoint-HEMCO and GC-Adjoint-STD.

https://doi.org/10.5194/gmd-2023-4
Preprint. Discussion started: 9 March 2023

Geoscientific Model Development
Discussions

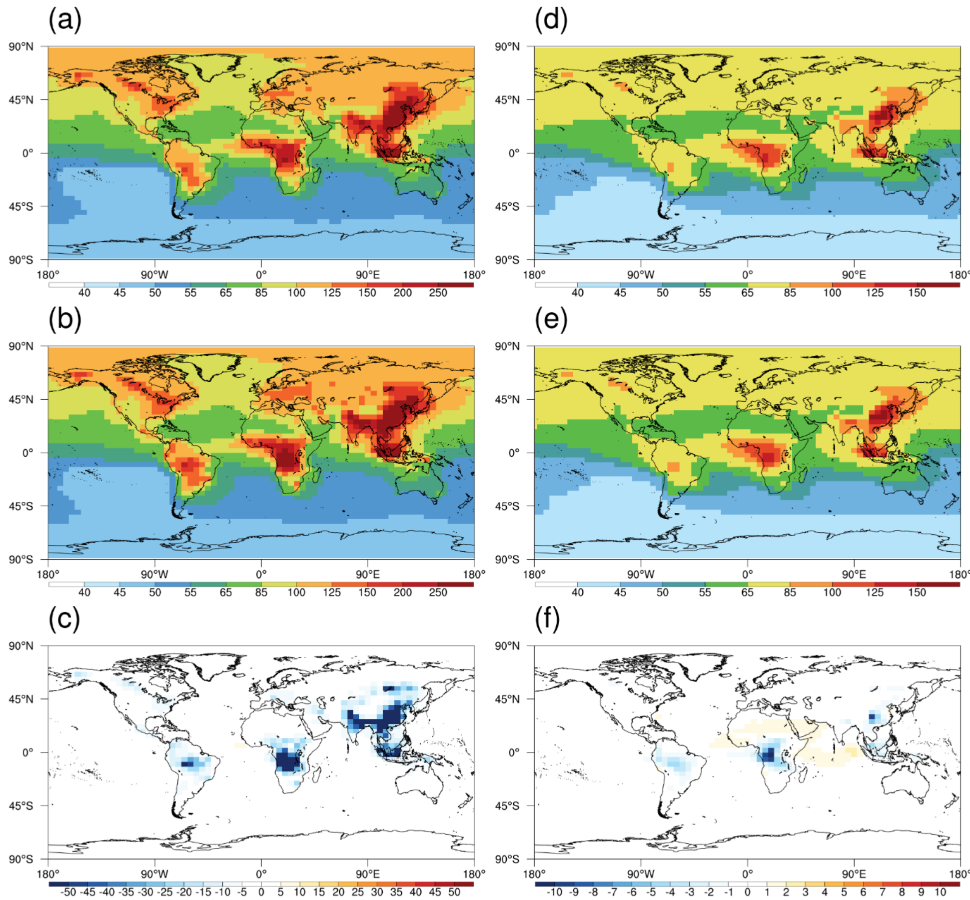

Fig. 4. Averages of surface CO concentrations in 2015 from (a) GC-Adjoint-HEMCO driven by MERRA-2, (b) GC-Adjoint-HEMCO driven by GEOS-FP and (c) their difference; (d-f) same as panels a-c, but for CO columns.

https://doi.org/10.5194/gmd-2023-4
Preprint. Discussion started: 9 March 2023

Geoscientific Model Development
Discussions

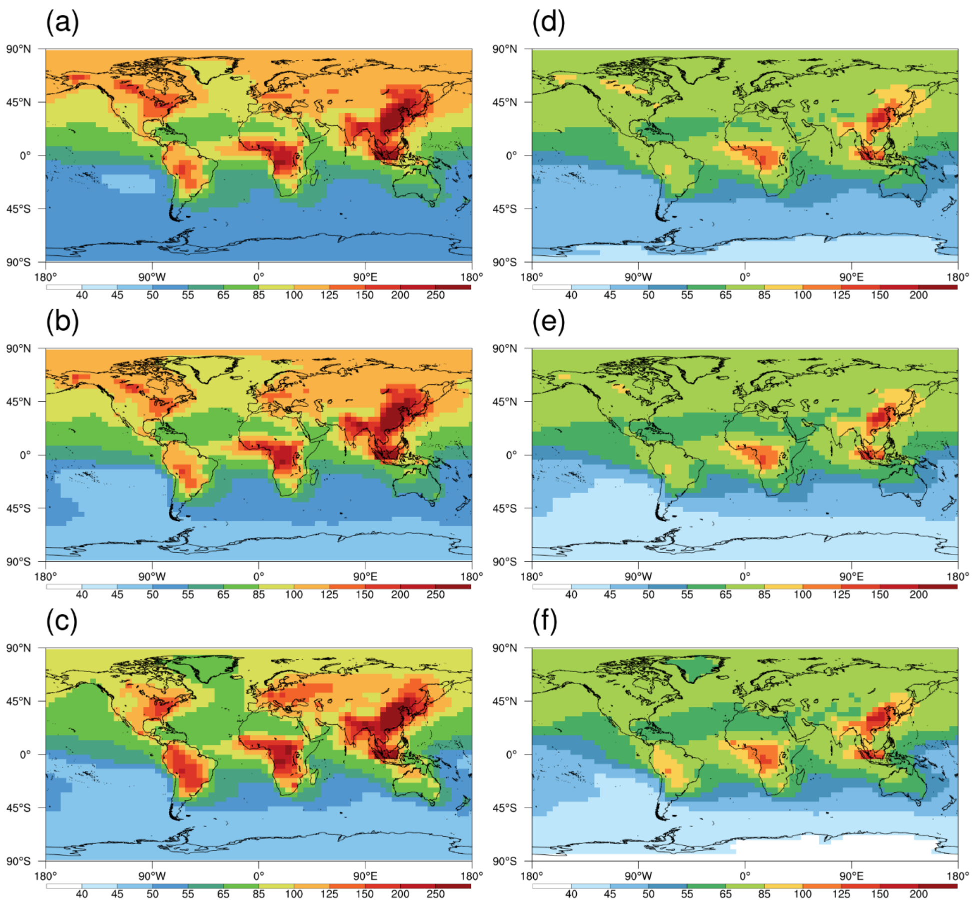

Fig. 5. Averages of surface CO concentrations in 2015 from (a) GC-v12; (b) GC-Adjoint-HEMCO; (c) GC-Adjoint-STD. (d-f) same as panels a-c, but for CO columns.

https://doi.org/10.5194/gmd-2023-4
Preprint. Discussion started: 9 March 2023

Geoscientific Model Development
Discussions

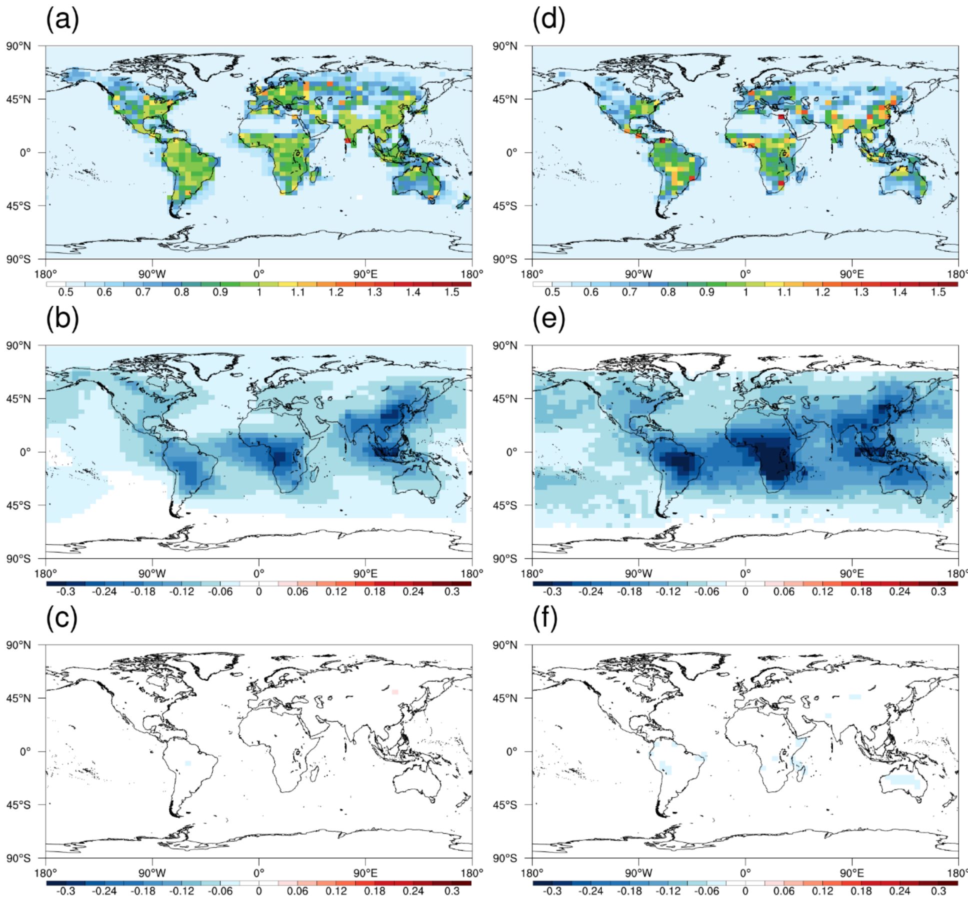

Fig. 6. (a) Annual scaling factors in OSSE-FullOBS. The scaling factors represent the ratio of the estimated to true emissions. The ratio for the first guess is 0.5. The actual value is 1.0. (b-c) the a priori and a posteriori biases calculated by (model-observation)/observation in OSSE-Full. (d-f) same as panels a-c, but for OSSE-MOPITT.

Geoscientific Model Development Discussions

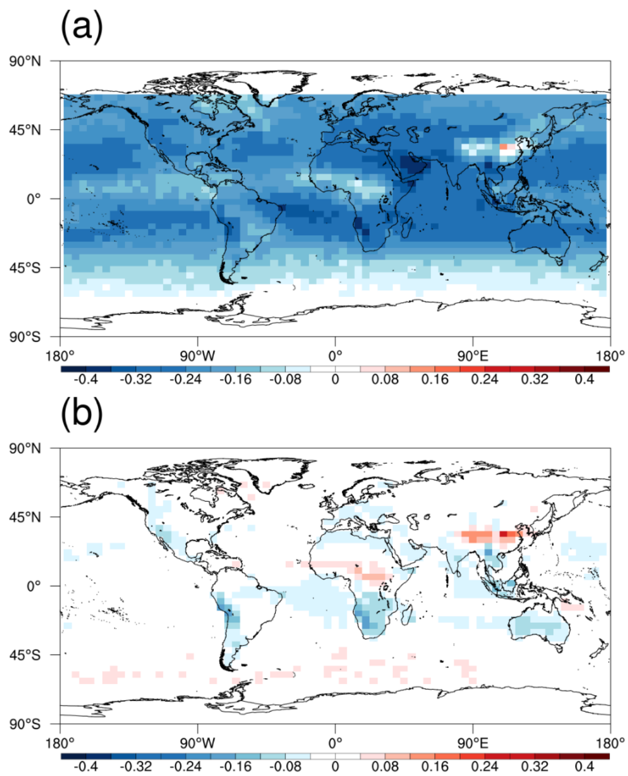

Fig. 7. (a) Biases in monthly initial CO conditions in 2015 in the original GEOS-Chem simulation. (b) same as panel a, but with optimized initial CO conditions provided by suboptimal sequential Kalman filter. The biases are calculated by (model-MOPITT)/MOPITT.

https://doi.org/10.5194/gmd-2023-4
Preprint. Discussion started: 9 March 2023

Geoscientific Model Development
Discussions

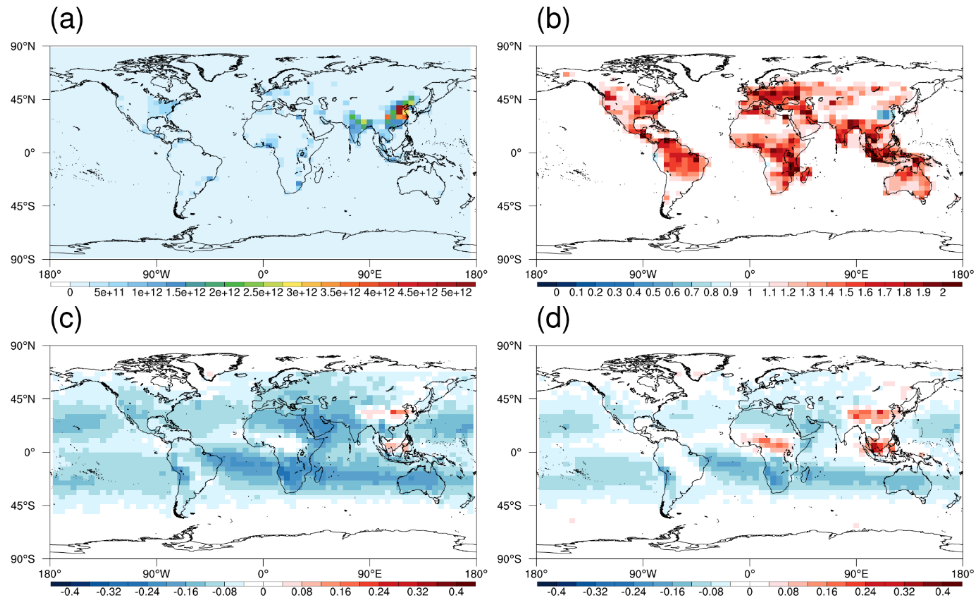

Fig. 8. (a) A priori anthropogenic CO emissions in 2015 with unit molec/cm^2/s; (b) Annual scaling factors for CO emissions in 2015. The scaling factors represent the ratio of the estimated to true emissions. (c-d) the a priori and a posteriori biases calculated by (model-MOPITT)/MOPITT.